

A Parameterized Physics-Informed Neural Network Solver for the Navier–Stokes Equations Across Reynolds Numbers

A. Jangir,^{1, a)} R. Clements,² R. Goyal,¹ and G. Tabor^{2, b)}

¹⁾*Department of Energy Science and Engineering, IIT Delhi*

²⁾*Department of Engineering, FESE, University of Exeter*

(Dated: 5 February 2026)

Physics-informed neural networks (PINNs) provide a mesh-free framework for solving partial differential equations by embedding governing physical laws directly into the training process. However, most PINNs developed for fluid dynamics remain restricted to fixed flow parameters, requiring retraining for each new condition and limiting their usefulness as general-purpose solvers. In this work, we develop a parameterized PINNs formulation for the incompressible Navier–Stokes equations in which the Reynolds number (Re) is treated as an explicit network input, enabling a single trained model to represent a continuous family of flow solutions. The approach is demonstrated using the 2D lid-driven cavity flow as a canonical benchmark. For low Re , where the flow is laminar and diffusion dominated, pure PINNs trained solely using the governing equations and boundary conditions accurately reproduce velocity and pressure fields across a wide range of Re , including cases not explicitly sampled during training. As the Re increases and the flow becomes increasingly convection dominated, the predictive accuracy of pure PINNs deteriorates due to stiffness and optimization imbalance. To address this limitation, a hybrid framework is introduced that combines transfer learning with sparse supervision from high-fidelity computational fluid dynamics (CFD) data. The resulting parameterized PINNs model accurately captures the Re dependence of the flow over both interpolation and limited extrapolation regimes while requiring CFD data only over a narrow subset of the parameter space. Detailed comparisons with OpenFOAM simulations demonstrate strong agreement in velocity profiles, and pressure fields. The results show that incorporating governing parameters directly into PINNs enables the construction of parametric Navier–Stokes solvers, offering a promising route toward efficient reduced-order modeling and data-assisted simulation of fluid flows.

I. INTRODUCTION:

The lid-driven cavity (LDC) flow is one of the most fundamental benchmark problems in fluid dynamics and has long served as a reference configuration for studying incompressible viscous flows and validating numerical methods. Owing to its geometric simplicity, well-defined boundary conditions, and strong sensitivity to the Reynolds number, the LDC flow remains a canonical test case for assessing numerical accuracy, stability, and convergence properties of Navier-Stokes solvers¹. Despite its simplicity, the flow exhibits rich physical behavior, including primary recirculation, secondary corner vortices, and pronounced changes in flow topology as the Reynolds number increases, making it particularly suitable for investigating parametric flow dependence.

Seminal benchmark solutions for the two-dimensional incompressible LDC flow were provided by Ghia *et al.*², who employed a multigrid finite-difference method to compute highly resolved velocity and streamfunction fields over a wide range of Reynolds numbers. Their centerline velocity profiles and vortex strength data have since become standard references for validating CFD solvers. Botella and Peyret³ later extended this work using a high-order Chebyshev collocation method with a regularized lid velocity profile, producing spectral benchmark solutions that remain definitive references for numerical accuracy assessment. Further advances were reported by Erturk *et al.*^{4,5}, who introduced compact high-

order finite-difference schemes and provided detailed analyses of convergence behavior and secondary vortical structures at higher Reynolds numbers. These studies firmly established the LDC flow as a stringent benchmark for incompressible Navier-Stokes solvers.

In contrast to conventional discretization-based methods, Raissi, Perdikaris, and Karniadakis⁶ introduced the physics-informed neural networks framework, in which the governing equations and boundary conditions are embedded directly into the training of neural networks through physics-based loss functions. This approach enables mesh-free solution of partial differential equations and has attracted significant attention within the fluid dynamics community for applications ranging from canonical laminar flows to turbulence modeling and multiphysics systems^{7–10}. At low Reynolds numbers, the flow is steady and laminar, characterized by a dominant central vortex and weaker secondary vortices near the corners. As the Reynolds number increases, nonlinear convective effects become increasingly important, leading to stronger velocity gradients, enhanced secondary structures, and, in three-dimensional configurations, transition toward unsteady and turbulent flow. These features have made the LDC problem a cornerstone in CFD, numerical analysis, and, more recently, data-driven and machine-learning-based approaches for fluid flows, including physics-informed neural networks and hybrid CFD-ML methods^{11–13}.

Building on the original PINNs formulation, numerous extensions have been proposed to improve convergence, robustness, and accuracy for Navier-Stokes problems. Kharazmi, Zhang, and Karniadakis¹⁴ introduced the hp-variational PINNs (hp-VPINNs) framework, combining domain decomposition with weak formulations to mitigate training stiffness

^{a)}Electronic mail: adityajangir873@gmail.com

^{b)}Electronic mail: g.r.tabor@exeter.ac.uk

at higher Reynolds numbers. Li and Feng¹⁵ proposed adaptive loss-weighting strategies to balance competing residual terms, while Chen and Zhao¹⁶ enhanced the performance of hard-constrained gradient-enhanced physics-informed neural networks (gPINNs) by employing a residual adaptive sampling strategy.

More recently, transfer learning has emerged as an effective strategy for improving the efficiency and robustness of PINNs when solving families of related flow problems. Wang *et al.*¹⁷ demonstrated that transfer learning can significantly reduce training cost while maintaining accuracy across variations in boundary conditions, material properties, and geometries. Related ideas have also been explored in broader data-driven modeling of fluid flows¹⁸, highlighting the potential of reusing learned representations. However, most existing transfer-learning studies remain focused on fixed-parameter settings, with limited capability for continuous parametric prediction.

In parallel, increasing attention has been devoted to parametric neural-network-based solvers, in which physical or geometric parameters are explicitly incorporated into the network inputs to enable learning of generalized solution manifolds. Such approaches have been investigated for surrogate modeling and reduced-order modeling of fluid flows. Sun *et al.*¹⁹ introduced parameterized PINNs for problems involving variable material properties, while Meng *et al.*²⁰ developed multi-task PINNs capable of solving families of partial differential equations with shared structure. Jagtap and Karniadakis²¹ emphasized the importance of parameter embedding and adaptive representations for mitigating spectral bias and improving generalization.

In fluid dynamics, explicit treatment of governing non-dimensional parameters is particularly important, as these parameters dictate the balance of physical mechanisms in the flow. The Reynolds number, in particular, controls the relative importance of convection and diffusion in the Navier-Stokes equations and directly influences flow topology, stability, and vortex formation. Training separate PINNs for individual Reynolds numbers not only increases computational cost but also prevents the model from learning the continuous dependence of the solution on governing parameters.

In the present work, a parameterized PINNs framework is developed for the lid-driven cavity flow by integrating Reynolds-number parameterization with transfer learning and sparse CFD supervision. The LDC flow is employed as a canonical testbed rather than the target application. The approach is examined across both low and high Reynolds number regimes and demonstrates that a single unified model can accurately predict velocity and pressure fields across a wide range of Reynolds numbers.

II. METHODOLOGY

A. Computational Fluid Dynamics (CFD)

1. Problem Statement and Boundary Conditions

The canonical two-dimensional lid-driven cavity problem is selected as the benchmark test case. The computational domain is a square cavity of dimension 1×1 . The top wall (lid) moves with a uniform velocity U_{lid} in the positive x direction, while the remaining three walls are at no-slip condition. This configuration induces a primary recirculating vortex within the cavity, with additional secondary vortices appearing near the corners as the Reynolds number increases. The governing equations for incompressible, viscous, and laminar steady flow consist of the continuity and Navier-Stokes equations. The continuity equation is expressed as

$$\nabla \cdot \mathbf{u} = 0 \quad (1)$$

and the steady-state Navier-Stokes equation in vector form is written as

$$(\mathbf{u} \cdot \nabla) \mathbf{u} = -\nabla p + \frac{1}{Re} \nabla^2 \mathbf{u} \quad (2)$$

where $\mathbf{u} = (u, v)$ denotes the velocity vector, p is the pressure, and $Re = \frac{U_{\text{lid}} L}{v}$ is the Reynolds number, defined in terms of the characteristic length L , lid velocity U_{lid} , and kinematic viscosity v .

Expanding the equations in component form for a two-dimensional flow (in the x - y plane), the governing equations become:

Continuity equation:

$$\frac{\partial u}{\partial x} + \frac{\partial v}{\partial y} = 0 \quad (3)$$

Momentum equations:

$$u \frac{\partial u}{\partial x} + v \frac{\partial u}{\partial y} = -\frac{\partial p}{\partial x} + \frac{1}{Re} \left(\frac{\partial^2 u}{\partial x^2} + \frac{\partial^2 u}{\partial y^2} \right) \quad (4)$$

$$u \frac{\partial v}{\partial x} + v \frac{\partial v}{\partial y} = -\frac{\partial p}{\partial y} + \frac{1}{Re} \left(\frac{\partial^2 v}{\partial x^2} + \frac{\partial^2 v}{\partial y^2} \right) \quad (5)$$

The incompressible Navier-Stokes equations are written in non-dimensional form, where the Reynolds number appears as the sole governing parameter controlling the relative importance of convective and diffusive effects. This non-dimensional formulation highlights the fundamental role of the Reynolds number in determining flow regimes and solution behavior, consistent with classical fluid mechanics theory^{22,23}.

2. Validation of CFD results from existing literature

CFD simulations were performed using the open-source finite-volume solver OpenFOAM 12. High-fidelity CFD solutions obtained using OpenFOAM are used as reference data

for validation. OpenFOAM has been extensively validated for incompressible laminar cavity flows and is widely used in benchmark CFD studies^{24,25}. A uniform computational grid consisting of 128×128 cells was employed, consistent with the grid resolution adopted in previous benchmark studies by Ghia *et al.*², Botella and Peyret³, and Erturk *et al.*^{4,5}. Erturk *et al.* demonstrated that this level of resolution is sufficient to accurately capture the dominant flow structures and secondary vortices within the cavity for Reynolds numbers up to approximately 10^3 .

The computed velocity profiles along the vertical centerline of the cavity for $Re = 100, 400$ and 1000 show good agreement with the benchmark data of Cortes and Miller²⁶, as illustrated in Fig. 1. Consequently, the CFD results obtained from this setup are considered reliable and are subsequently used as the ground truth for validating the PINNs predictions.

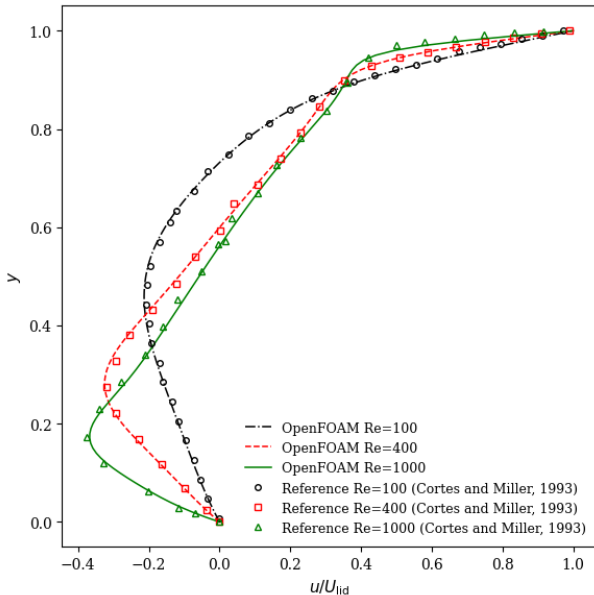


FIG. 1. Comparison of horizontal velocity u/U_{lid} along the vertical centerline ($x = 0.5$) between OpenFOAM 12 results and reference data of Cortes and Miller (1993) at $Re = 100, 400$ and 1000 .

B. Physics-Informed Neural Networks (PINNs)

1. Neural Network Architecture

A fully connected feed-forward neural network (FNN) is employed to approximate the velocity and pressure fields within the cavity, as schematically illustrated in Fig. 2. The network takes three input features: the spatial coordinates (x, y) and the Reynolds number (Re). Treating the Reynolds number as an explicit input parameter enables parametric generalization, allowing the network to learn a continuous solution manifold spanning multiple flow regimes. As shown in the figure, this parametric formulation allows a single neural network to represent solutions corresponding to different

Reynolds numbers. Such parameterized PINN approaches have been shown to be effective for solving families of partial differential equations with shared physical structure and for enabling predictive capability beyond fixed boundary conditions^{19,20,27}.

To ensure numerical stability and efficient learning, the Reynolds number input is transformed using a logarithmic mapping and subsequently normalized, as indicated in the input layer of Fig. 2. This logarithmic transformation compresses the wide dynamic range of Reynolds numbers and prevents it from dominating the spatial inputs. Moreover, this choice is particularly well suited to the hyperbolic tangent (\tanh) activation function employed in the hidden layers. Since \tanh exhibits its highest sensitivity and gradient magnitude near zero and rapidly saturates for large input values, centering the log-transformed Reynolds number around zero ensures that the activations remain within the linear regime of \tanh , thereby mitigating vanishing-gradient issues and improving convergence during training.

As depicted in Fig. 2, the network outputs the two velocity components (u, v) and the pressure field p . The architecture consists of ten hidden layers ($H = 10$) with eighty neurons per layer ($N = 80$). Hyperbolic tangent (\tanh) activation functions are employed due to their smoothness, bounded output, and suitability for representing continuous physical fields governed by partial differential equations^{6,28}. The symmetric output range of \tanh further promotes balanced gradient flow and improved training stability, which is particularly beneficial in physics-informed learning frameworks²¹.

To train the parametric PINNs across a range of flow regimes, Reynolds numbers are sampled within the training interval using a logarithmic-uniform distribution, as illustrated in the Reynolds-number sampling block of Fig. 2. Logarithmic-uniform sampling ensures balanced coverage across the Reynolds-number space and provides uniform representation in log-space, which is consistent with the logarithmic input transformation. This strategy prevents oversampling at high Reynolds numbers and enhances the network's ability to learn smooth parametric dependencies on Re .

Network weights are initialized using the Glorot (Xavier) initialization scheme to preserve the variance of activations and gradients across layers, thereby mitigating vanishing or exploding gradient issues and facilitating stable convergence during training²⁹. For the pure PINNs configuration, the training process illustrated in Fig. 2 relies exclusively on physics-based constraints. During backpropagation, gradients of this total loss with respect to the network parameters (\mathbf{w}, \mathbf{b}) are computed, and the weights are updated using gradient-based optimization. Through this update, the network progressively adjusts its parameters so that the predicted fields simultaneously satisfy the governing physical laws and boundary conditions.

This process constitutes one training cycle. Repeating this cycle over many iterations enables the PINNs to minimize the residuals of the Navier-Stokes equations across the sampled Reynolds-number space. As a result, the trained network learns a parametric solution manifold that enforces the underlying physics while generalizing smoothly across different

Reynolds numbers within the training range. The selected network depth and width provide sufficient expressive capacity to capture the nonlinear flow features present in the lid-driven cavity flow across the considered range of Reynolds numbers.

2. Computational Domain

The computational domain consists of a two-dimensional square cavity of size 1×1 . Within this domain, N_f interior collocation points and N_b boundary points are distributed, as illustrated in Fig. 3. Several sampling strategies were evaluated, including Latin Hypercube sampling, Sobol low-discrepancy sequences, uniform grid sampling, and Monte Carlo sampling. Based on comparative testing, Monte Carlo sampling was selected for the final implementation due to its favorable balance between accuracy, robustness, and computational efficiency.

The collocation points are sampled independently from a uniform distribution over the domain $\Omega = [x_{\min}, x_{\max}] \times [y_{\min}, y_{\max}]$, such that

$$(x_i, y_i) \sim \mathcal{U}(\Omega) \quad (6)$$

The physics-informed residual loss can be interpreted as an integral over the computational domain,

$$\mathcal{L} = \int_{\Omega} \|R(\mathbf{x})\|^2 d\mathbf{x} \quad (7)$$

where $R(\mathbf{x})$ denotes the governing equation residuals. In practice, this integral is approximated using a Monte Carlo estimator,

$$\widehat{\mathcal{L}} = \frac{1}{N_f} \sum_{i=1}^{N_f} \|R(\mathbf{x}_i)\|^2 \quad (8)$$

which provides an unbiased estimate with a convergence rate of $\mathcal{O}(N_f^{-1/2})$, independent of dimensionality.

Compared to structured grids, random sampling mitigates aliasing effects and grid-induced artifacts, particularly when the residual field contains high-frequency components. The stochasticity introduced by Monte Carlo sampling also benefits gradient-based optimization by improving exploration of the loss landscape^{6,30}. During training, the Adam optimizer is first employed to provide stochastic updates that enable rapid exploration and escape from shallow local minima³¹. Subsequently, the L-BFGS optimizer is applied for deterministic fine-tuning, exploiting the smoother loss surface achieved after Adam pre-training^{6,32}. The combined Monte Carlo sampling and Adam-L-BFGS optimization strategy enhances convergence stability and accuracy, particularly for nonlinear, multiscale flows governed by competing convective and diffusive effects^{21,33}.

3. Hyperparameters

Training of the physics-informed neural network is performed in two stages. In the first stage, the Adam optimizer is

used to obtain a coarse approximation of the solution, providing suitable initial weights and biases for the network³¹. In the second stage, the L-BFGS optimizer is employed to further refine convergence and reduce the residuals of the governing equations^{6,32}. An adaptive learning rate strategy is adopted, starting from 10^{-3} and gradually decreasing to 10^{-6} to ensure stable convergence and prevent premature stagnation.

The number of hidden layers (H) and neurons per layer (N) are selected based on parametric studies that balance predictive accuracy and computational efficiency. A hyperbolic tangent activation function with Glorot initialization is used in all hidden layers, while the output layer employs a linear activation to directly represent the physical variables. This configuration provides a robust and expressive architecture for learning nonlinear flow fields within the PINNs framework.

4. Loss Function Design

The total loss function, \mathcal{L} , is defined as a weighted sum of the boundary condition loss and the PDE residual loss:

$$\mathcal{L} = \lambda_b \mathcal{L}_b + \lambda_{\text{PDE}} \mathcal{L}_{\text{PDE}} \quad (9)$$

where λ_b and λ_{PDE} are the respective weighting coefficients. These weights can be adjusted to balance the relative contributions of each term and prevent any single component from dominating the training process.

The PDE loss enforces the incompressible Navier-Stokes equations and continuity. The residuals of the governing equations are given by

$$\mathcal{R}_c = u_x + v_y \quad (10)$$

$$\mathcal{R}_u = u u_x + v u_y + p_x - \frac{1}{Re} (u_{xx} + u_{yy}) \quad (11)$$

$$\mathcal{R}_v = u v_x + v v_y + p_y - \frac{1}{Re} (v_{xx} + v_{yy}) \quad (12)$$

where subscripts denote partial derivatives and Re is the Reynolds number. The PDE loss is defined as the mean squared error (MSE) of these residuals over the collocation points:

$$\mathcal{L}_{\text{PDE}} = \frac{1}{N_f} \sum_{i=1}^{N_f} (|\mathcal{R}_c|^2 + \mathcal{R}_u^2 + \mathcal{R}_v^2) \quad (13)$$

where N_f is the number of collocation points. The PDE residuals were computed using automatic differentiation, thereby embedding the governing physical laws directly into the training process.

The boundary condition loss enforces the no-slip and lid-driven conditions at the cavity walls:

$$\mathcal{L}_b = \frac{1}{N_b} \sum_{i=1}^{N_b} \left[(u_i^{\text{pred}} - u_i^{\text{bc}})^2 + (v_i^{\text{pred}} - v_i^{\text{bc}})^2 \right] \quad (14)$$

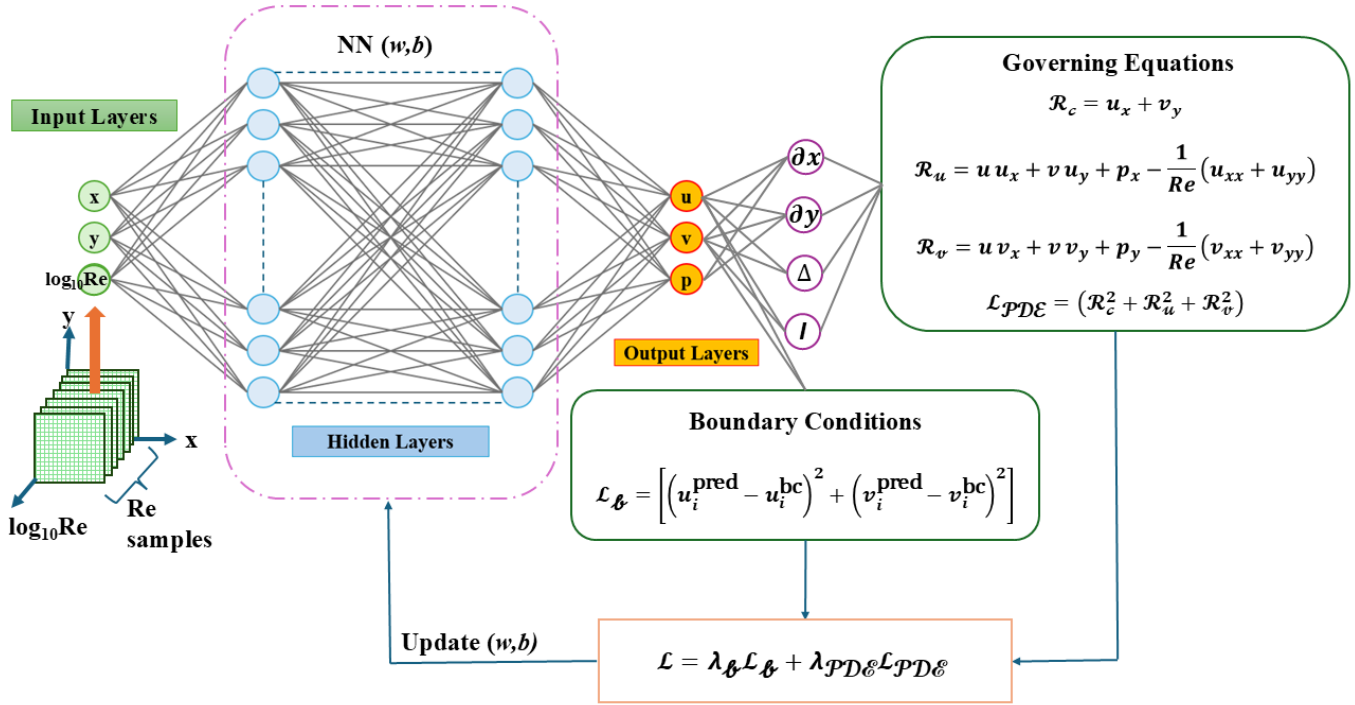


FIG. 2. Schematic of the fully connected feed-forward neural network architecture used in this study.

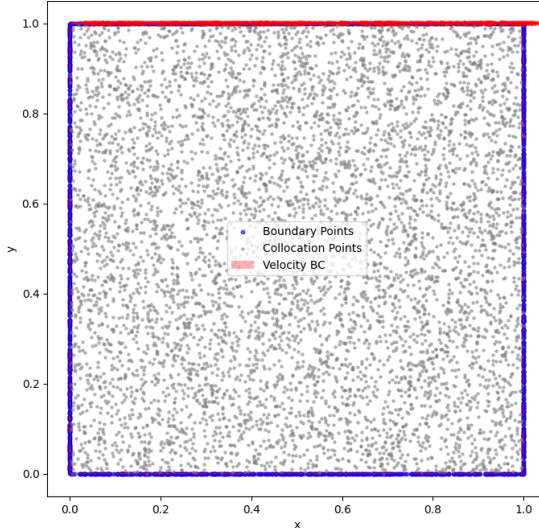


FIG. 3. Randomly distributed collocation (N_f) and boundary (N_b) points within the 1×1 cavity domain.

where u_i^{pred} and v_i^{pred} are the predicted velocities at boundary point i , u_i^{bc} and v_i^{bc} are the prescribed boundary values, and N_b is the number of boundary points.

The PINNs framework embeds the governing Navier-Stokes equations and boundary conditions directly into the loss function by penalizing the residuals at collocation points. This formulation follows the original PINNs methodology in-

roduced by Raissi *et al.*⁶ and later reviewed comprehensively by Karniadakis *et al.*³⁰.

This formulation, normalized by the number of collocation and boundary points, ensures that the PINNs solution simultaneously satisfies the governing equations and the prescribed boundary conditions. Several studies have examined the convergence behavior and theoretical properties of PINNs, identifying challenges associated with complex optimization landscapes and limited network expressivity^{34,35}.

5. Gradient Norm Analysis

During the training of PINNs, monitoring the gradient norm is a useful way to evaluate the stability and balance of the optimization process. The gradient norm measures the overall size of the gradients of each loss term with respect to the trainable parameters of the neural network. Tracking this quantity helps detect common training issues such as vanishing gradients, exploding gradients, or imbalance between different loss components.

Imbalanced gradient norms can slow down or prevent convergence in PINNs, especially for convection-dominated problems^{33,36}. For each loss component \mathcal{L}_i , such as the PDE residual loss or the boundary condition (BC) loss, the gradient with respect to the network parameters θ is denoted by $\nabla_{\theta}\mathcal{L}_i$. The corresponding ℓ_2 -norm of this gradient, referred to as the

gradient norm, is defined as

$$\|g\| = \|\nabla_{\theta} \mathcal{L}_i\|_2 = \sqrt{\sum_{j=1}^{N_{\theta}} \left(\frac{\partial \mathcal{L}_i}{\partial \theta_j} \right)^2} \quad (15)$$

where N_{θ} is the total number of trainable parameters in the neural network.

At each training iteration, the gradient norms of the different loss components are computed using automatic differentiation. Comparing these values allows us to assess the relative contribution of each physical constraint to the parameter updates. If one loss term has a much larger gradient norm than the others, it can dominate the training process and lead to an unbalanced solution. In such cases, loss reweighting or adaptive training strategies can be used to restore balance among the different loss terms.

The evolution of the gradient norms during training is recorded and analyzed to ensure that the optimization remains stable and avoids vanishing or exploding gradients. This analysis provides insight into the training dynamics and helps guide the selection of learning rates, loss weights, and optimizer settings in the PINNs framework.

III. RESULTS AND DISCUSSION

A. Low Reynolds Number (Pure PINNs)

In this section, the performance of the proposed PINNs framework is assessed for low-Reynolds-number lid-driven cavity flows, with Reynolds numbers up to $Re = 300$. It is emphasized that the PINNs model is trained without the use of any CFD data. Instead, learning is driven solely by the governing physics, enforced through the incompressible Navier-Stokes equations and the associated boundary conditions.

Because no data-driven loss terms or external solution samples are incorporated during training, the present approach is referred to as *pure PINNs*. This setting provides a stringent test of the model's ability to recover physically consistent flow solutions based exclusively on the embedded physical constraints.

To assess the accuracy and physical fidelity of the pure PINNs predictions, reference solutions are generated using the open-source finite-volume CFD solver OpenFOAM 12. These high-quality CFD results are used as the reference solution for comparison. They allow a clear evaluation of how well the model predicts the velocity and pressure fields at different Reynolds numbers. By comparing the PINNs results with the benchmark CFD solutions, we can clearly show how effective the physics-informed learning approach is at capturing the main flow features without using any training data.

1. Effect of Sampling Strategies on PINNs Performance

To evaluate the influence of collocation-point sampling strategies on the performance of PINNs, four different methods were examined: Latin Hypercube sampling, Monte Carlo

sampling, Sobol low-discrepancy sampling, and a uniform (structured) grid. Each sampling method was trained over the considered range of Reynolds numbers and then tested for the lid-driven cavity flow at $Re = 100$. To ensure a fair comparison, the same neural network architecture, identical hyperparameters, and the same number of collocation and boundary points were used for all sampling methods. The convergence behavior, computational cost, and prediction accuracy were compared, and the key results are summarized in Table I.

Among the sampling strategies examined, the Sobol sequence exhibited the fastest convergence to the prescribed residual tolerance of 10^{-3} , requiring approximately 37,000 training epochs. Latin hypercube sampling (LHS) also demonstrated satisfactory convergence behavior, albeit at a higher computational cost. In contrast, the uniform grid showed the slowest convergence and failed to reach the target residual level within 150,000 epochs.

Prediction accuracy was measured using the percentage error between the PINNs-predicted and CFD benchmark u -velocity along the vertical centerline ($x = 0.5$). Using this metric, Latin Hypercube Sampling (LHS) achieved the highest accuracy, with a mean error of 1.01% and a maximum local error of 2.67%. Monte Carlo (MC) sampling gave moderate accuracy, with a mean error of 2.79%, while requiring far fewer training epochs than both the LHS and uniform grid methods. Although Sobol sampling converged the fastest, it produced the largest errors, with a mean error of 19.31%.

The lower accuracy of Sobol-based PINNs, despite its fast convergence, is due to the uniformity and low-discrepancy properties of Sobol points. These properties help minimize the global residual quickly but may provide insufficient resolution in areas with sharp gradients, such as near-wall boundary layers and corner vortices in the lid-driven cavity. As a result, the network converges to a solution that satisfies the governing equations in an overall sense but cannot capture fine local flow features accurately. This demonstrates that fast residual convergence does not always guarantee high prediction accuracy in PINNs.

Considering both accuracy and computational cost, Monte Carlo sampling provides the best balance. It achieves reasonable prediction accuracy while significantly reducing training time and computational effort. These advantages make it suitable for repeated PINNs training, parametric studies, and hyperparameter tuning. Therefore, Monte Carlo sampling is chosen as the preferred strategy for the rest of this study.

2. Loss Function Convergence

The convergence behavior of the total loss and its individual components is illustrated in Fig. 4. The total loss function consists of contributions from the governing equations (PDE loss) and the boundary conditions (BC loss), with the PDE loss further decomposed into the continuity loss and the momentum losses in the x - and y -directions, corresponding to the residuals of the Navier-Stokes equations. As shown in Fig. 4, the boundary loss exhibits a relatively higher magnitude compared to the PDE components during training, reflecting the

TABLE I. Comparison of sampling methods for PINNs training in the lid-driven cavity at $Re = 100$. Mean and maximum errors represent the percentage error in the predicted centerline u -velocity compared to CFD results.

Method	Epochs to reach 10^{-2} residual	Epochs to reach 10^{-3} residual	Time per 1000 epochs (s)	Mean Error (%)	Maximum Error (%)
Latin Hypercube	35000	120000	87.0	1.01	2.67
Monte Carlo	18000	62000	87.5	2.79	4.56
Sobol	16000	37000	88.5	19.31	29.63
Uniform Grid	83000	> 150000	86.5	5.20	8.51

stricter enforcement of boundary constraints. To ensure stable and balanced convergence, a piecewise-constant learning rate schedule was employed. The training started with an initial learning rate of 5×10^{-3} , which was gradually reduced at selected epochs, as summarized in Table II. A larger learning rate in the early stages facilitates rapid learning, while progressively smaller learning rates allow finer parameter updates as the solution converges. The dotted orange vertical lines in Fig. 4 mark the epochs at which the learning rate was adjusted, in accordance with the schedule listed in Table II.

The model was trained for a total of 500,000 epochs using the Adam optimizer during the initial phase to achieve fast descent, followed by the L-BFGS optimizer for high-precision fine-tuning of the network parameters. The gradual and smooth reduction of all loss components demonstrates the stable and physically consistent convergence behavior of the proposed PINNs framework for the lid-driven cavity flow case.

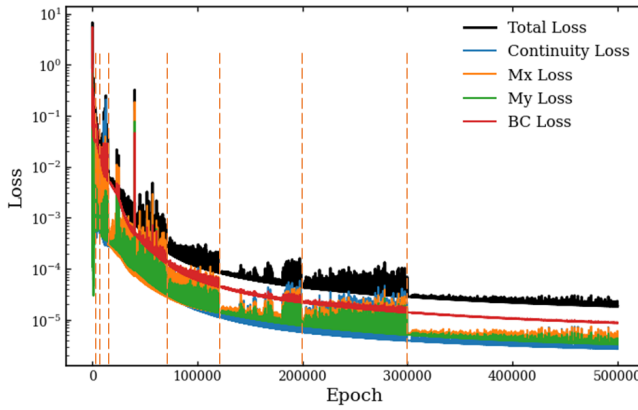


FIG. 4. Convergence history of the total loss and its individual components for the lid-driven cavity case. The dotted orange vertical lines indicate the epochs at which the learning rate was adjusted according to the schedule listed in Table II.

3. Gradient Norm Plot

To assess training stability and diagnose stiffness in the optimization process, gradient norm analysis is employed by monitoring the magnitude of gradients associated with different loss components. Figure 5 illustrates the variation of the gradient norm with respect to the number of training epochs.

TABLE II. A piecewise-constant learning rate schedule was used during PINNs training.

Epoch Range	Learning Rate
0 – 1,000	5×10^{-3}
1,001 – 5,000	1×10^{-3}
5,001 – 15,000	5×10^{-4}
15,001 – 70,000	1×10^{-4}
70,001 – 120,000	5×10^{-5}
120,001 – 200,000	1×10^{-5}
200,001 – 300,000	5×10^{-6}
> 300,000	1×10^{-6}

The gradient norm provides insight into the stability of the optimization process and the learning capability of the network. At the beginning of the training, the gradient norm lies within the healthy range of 10^{-3} to 10^1 , indicating an adequate magnitude of gradients for effective parameter updates. This range ensures that the network learns efficiently without experiencing gradient explosion or vanishing.

During training, the gradient norm gradually decreases, showing that the optimizer is moving toward a local minimum of the loss. However, after about 150,000 epochs, the gradient norm drops below 10^{-4} , leaving the healthy range. This indicates the onset of the gradient vanishing problem, where the parameter updates become extremely small. As a result, the training slows down and eventually stagnates, which is reflected by the plateau in the total loss shown in Fig. 4. At this point, the loss function is almost flat, and further training does not significantly improve the model's accuracy.

The observed trend suggests that extending the training beyond this point provides diminishing returns while increasing computational cost. Therefore, it is recommended to terminate the training after a few hundred thousand epochs once the gradient norm approaches the lower bound of the healthy region. Monitoring the gradient norm thus serves as a practical criterion for early stopping, preventing unnecessary computations and ensuring efficient use of computational resources.

4. Contours of u , v , and p

The predicted velocity and pressure contours reveal the formation of a dominant primary vortex and progressively stronger secondary corner vortices as the Reynolds number increases. These flow features are consistent with classical numerical and experimental studies of the lid-driven cavity flow^{1-3,5}.

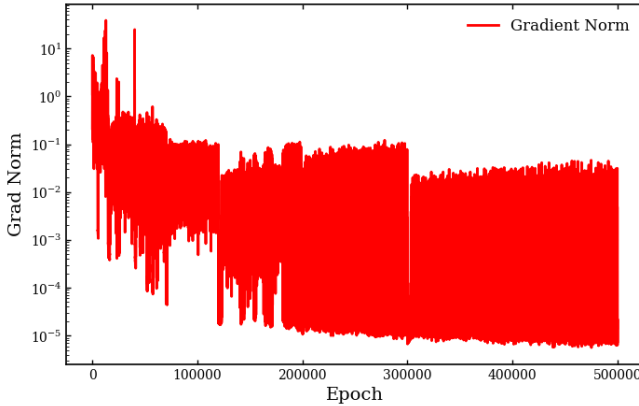


FIG. 5. Evolution of gradient norms during training for pure PINNs at different Reynolds numbers. Large imbalances in gradient magnitudes indicate training stiffness, consistent with known optimization pathologies in PINNs^{33,36}.

The contour plots for the lid-driven cavity flow at Reynolds numbers $Re = 50, 100, 150$, and 200 are presented in Figures 6 and 7. Figure 6 illustrates the horizontal velocity component (u), where each row corresponds to a different Reynolds number and compares the PINNs predictions with the reference OpenFOAM (ground truth) solution. The absolute error between the two fields is also included to highlight the regions of discrepancy. The contours provide a direct comparison between the PINNs model predictions and the reference solution obtained from OpenFOAM. The well-trained PINNs model is capable of predicting the velocity and pressure at any given point by inputting its spatial coordinates and the Re . The largest discrepancies are observed near the upper left and right corners of the cavity, where abrupt variations in the boundary conditions lead to localized errors. Figure 7 presents the vertical velocity component (v) and pressure field (p) for the same Reynolds numbers. Similar to Figure 6, each subplot provides a side-by-side comparison of the PINNs results, the OpenFOAM benchmark, and the corresponding absolute error distribution.

It is evident that the PINNs model demonstrates strong agreement with the CFD results across all Reynolds numbers considered. The error concentrations are more noticeable near the top-left and top-right corners of the cavity, where sharp gradients occur due to the lid motion and the changing flow structures at higher Re values for vertical component of the velocity.

5. Velocity Profiles

Velocity profiles along the cavity centerlines are compared with CFD reference solutions following standard validation practices commonly adopted in lid-driven cavity benchmarks^{2,3}.

Figure 8 presents a quantitative comparison of velocity profiles between the PINNs predictions and the CFD reference solutions obtained using OpenFOAM 12 for the lid-driven cavity flow at $Re = 50$. The figure shows the horizontal veloc-

ity component (u) along selected vertical lines at $x = 0.2, 0.5$, and 0.8 , as well as the vertical velocity component (v) along selected horizontal lines at $y = 0.2, 0.5$, and 0.8 . Across all sampled locations, the PINNs predictions exhibit excellent agreement with the CFD results, accurately capturing the velocity distributions throughout the cavity. The error bars indicate $\pm 5\%$ of the CFD ground truth, demonstrating that the PINNs predictions remain well within the prescribed tolerance and confirming the robustness and accuracy of the proposed physics-informed framework in the low-Reynolds-number regime.

Figure 9 presents a quantitative comparison of velocity profiles between the PINNs predictions and the CFD reference solutions obtained using OpenFOAM 12 for the lid-driven cavity flow at $Re = 100$. The figure shows the horizontal velocity component (u) evaluated along selected vertical lines at $x = 0.2, 0.5$, and 0.8 , as well as the vertical velocity component (v) evaluated along selected horizontal lines at $y = 0.2, 0.5$, and 0.8 . Across all sampled locations, the PINNs predictions exhibit excellent agreement with the CFD results, accurately capturing the velocity gradients and flow symmetry within the cavity. The error bars indicate $\pm 5\%$ of the CFD ground truth, confirming that the predicted results remain within acceptable deviation limits and demonstrating strong consistency between the PINNs framework and the CFD simulations.

Figure 10 shows a quantitative comparison of velocity profiles obtained from the PINNs predictions and the CFD reference solutions computed using OpenFOAM 12 for the lid-driven cavity flow at $Re = 200$. The figure shows the horizontal velocity component (u) evaluated along selected vertical lines at $x = 0.2, 0.5$, and 0.8 , as well as the vertical velocity component (v) evaluated along selected horizontal lines at $y = 0.2, 0.5$, and 0.8 . The PINNs predictions demonstrate strong agreement with the CFD results across all sampled locations, accurately reproducing the velocity distributions and key flow features within the cavity at this higher Reynolds number. The error bars represent $\pm 10\%$ of the CFD ground truth, indicating that the PINNs predictions remain well within acceptable deviation limits and confirming the reliability of the proposed physics-informed framework across the computational domain.

6. Influence of Collocation-Point Density on Model Accuracy

To assess the sensitivity of the PINNs predictions to the density of training points, three spatial discretizations were employed: a coarse grid (3,300 points), a medium grid (5,200 points), and a fine grid (11,700 points). Each configuration contained both collocation points enforcing the governing equations and boundary points enforcing Dirichlet conditions. The prediction accuracy of the PINNs is quantified using the mean squared error (MSE) and the coefficient of determination (R^2), which are widely adopted performance metrics for physics-informed learning frameworks^{37,38}. The MSE measures the absolute discrepancy between the PINNs predictions and the CFD ground truth, with smaller values indicating

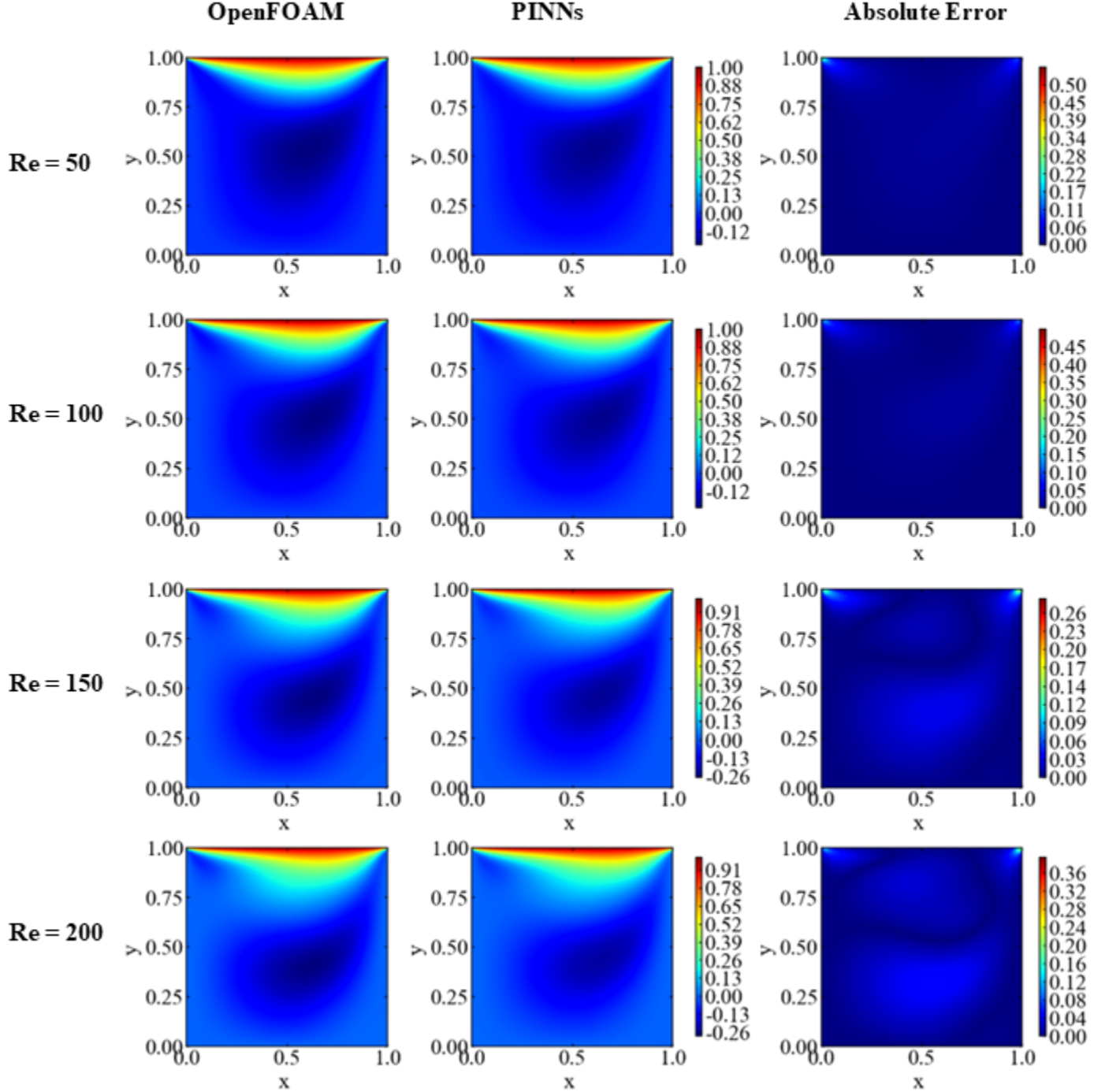


FIG. 6. Comparison of horizontal velocity (u) field between OpenFOAM (ground truth) and PINNs for lid-driven cavity flow at $Re = 50, 100, 150$, and 200 .

higher accuracy, while the R^2 metric quantifies the degree to which the predicted fields capture the variance of the reference solution. Values of R^2 approaching unity correspond to strong predictive agreement.

Table III summarizes the resulting MSE and R^2 for the u velocity field over Reynolds numbers in the range $Re = 50$ – 200 .

200.

The results indicate that the PINNs predictions exhibit limited sensitivity to grid refinement for low and moderate Reynolds numbers ($Re \leq 100$). Across these cases, the MSE values for the u velocity fields remain on the order of 10^{-4} for all three grids, and the corresponding R^2 values exceed

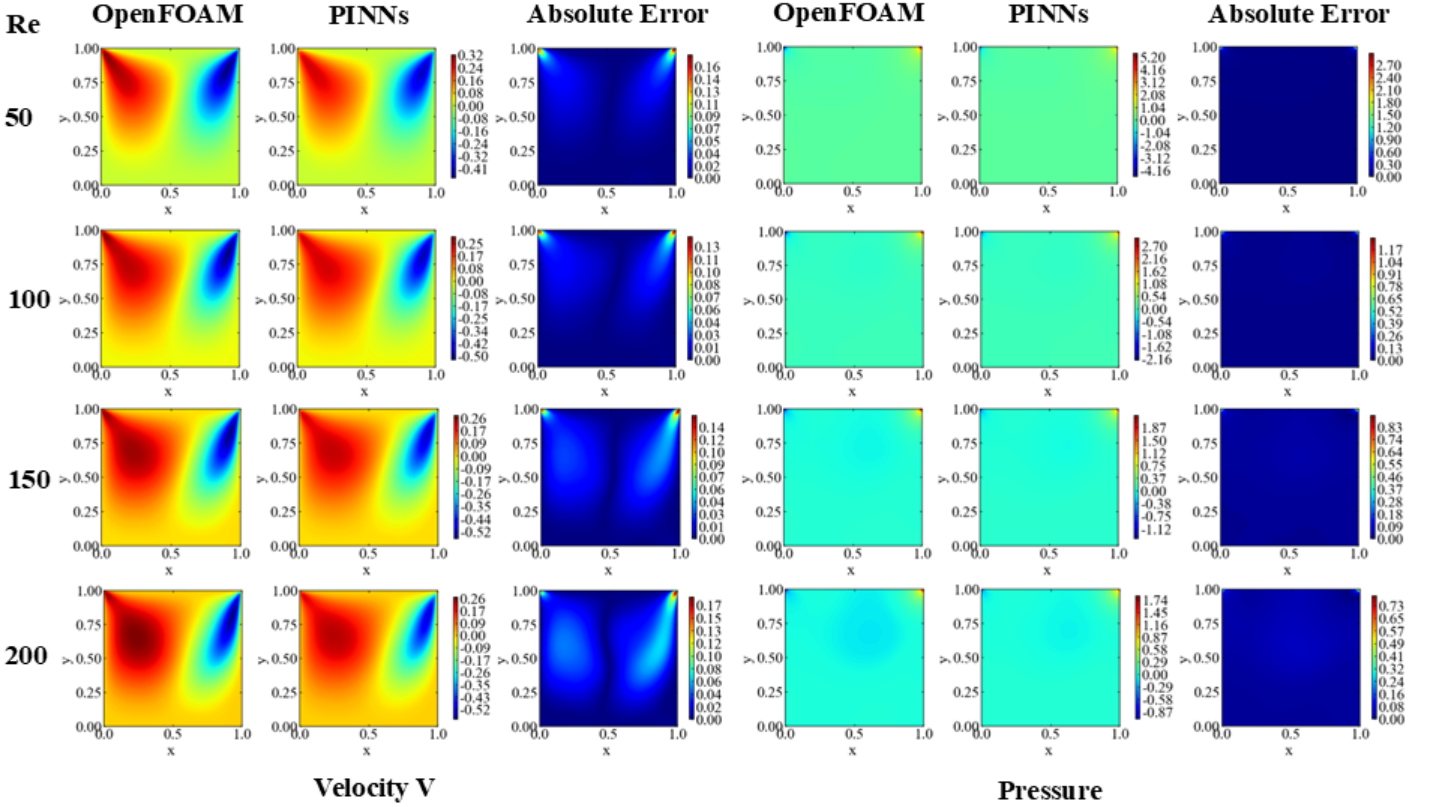


FIG. 7. Comparison of vertical velocity (v) and pressure (p) fields between OpenFOAM (ground truth) and PINNs for lid-driven cavity flow at $Re = 50, 100, 150$, and 200 .

0.96 even for the coarse discretization. This shows that PINNs can capture the flow physics accurately with a relatively small number of collocation points, demonstrating their data efficiency compared to traditional mesh-based CFD methods.

At higher Reynolds numbers ($Re = 150$ and 200), the effect of point density becomes more noticeable. The coarse grid shows higher MSE and lower R^2 values, especially at $Re = 200$, where R^2 drops to 0.8784. Increasing the number of collocation points improves both MSE and R^2 , with the fine grid achieving the best accuracy across all metrics. This behavior reflects the sharper velocity gradients and stronger nonlinearities at higher Reynolds numbers, which require more points to accurately resolve the PDE residuals.

Examination of the results confirm that PINNs maintain good accuracy even with a modest number of points, but finer grids improve predictions when the flow is more complex. The method generalizes well, achieving high accuracy with relatively few training points, while still benefiting from additional resolution when needed.

Figure 11 shows the effect of collocation-point density on the accuracy of PINNs predictions for the lid-driven cavity problem across a range of Reynolds numbers.

The left panel presents the MSE of the u velocity field. It can be observed that finer grids (11,700 points) consistently reduce the MSE compared to medium and coarse grids, particularly at higher Reynolds numbers where the flow exhibits

stronger nonlinearities. The coarse grid (3,300 points) exhibits higher MSE, whereas the medium grid (5,200 points) improves accuracy moderately.

The right panel shows the R^2 for the u velocity field predictions. Even for the coarse grid, R^2 remains above 0.95 for moderate Reynolds numbers ($Re \leq 100$), indicating that the PINNs effectively captures the essential flow physics. At higher Reynolds numbers ($Re = 150$ and 200), the fine grid provides noticeably better fidelity, reflecting the need for additional collocation points to resolve sharper velocity gradients.

In summary, these results highlight the influence of collocation-point density on model accuracy, while PINNs can achieve high accuracy with a moderate number of points, increasing the number of collocation points improves predictive performance at higher Reynolds numbers.

7. Model Accuracy: Comparison Between CFD and PINNs Predictions

To assess both the interpolation and extrapolation capabilities of the proposed PINNs framework, the model predictions were compared against high-fidelity CFD solutions at multiple Reynolds numbers. The Reynolds number range used for model training, $50 \leq Re \leq 300$, is defined as the *interpol-*

TABLE III. Effect of collocation-point density on PINNs accuracy. Mean squared error (MSE) and coefficient of determination (R^2) for coarse (3,300 points), medium (5,200 points), and fine (11,700 points) grids across different Reynolds numbers.

Re	MSE			R^2		
	Coarse	Medium	Fine	Coarse	Medium	Fine
50	1.78×10^{-4}	1.88×10^{-4}	1.96×10^{-4}	0.9860	0.9832	0.9846
80	8.37×10^{-4}	6.38×10^{-4}	1.98×10^{-4}	0.9740	0.9863	0.9939
100	1.77×10^{-3}	1.19×10^{-3}	2.17×10^{-4}	0.9647	0.9768	0.9937
150	7.07×10^{-3}	5.19×10^{-3}	1.93×10^{-3}	0.9571	0.9534	0.9827
200	2.42×10^{-2}	1.18×10^{-2}	1.11×10^{-2}	0.8784	0.9093	0.9442

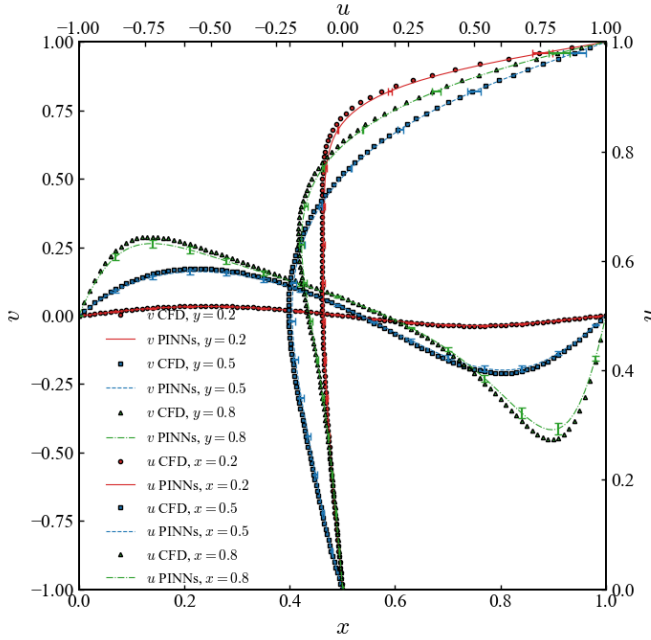


FIG. 8. Comparison of u -velocity profiles along vertical lines ($x = 0.2, 0.5, 0.8$) and v -velocity profiles along horizontal lines ($y = 0.2, 0.5, 0.8$) between PINNs predictions and OpenFOAM 12 results at $Re = 50$. Error bars represent $\pm 5\%$ of the CFD ground truth.

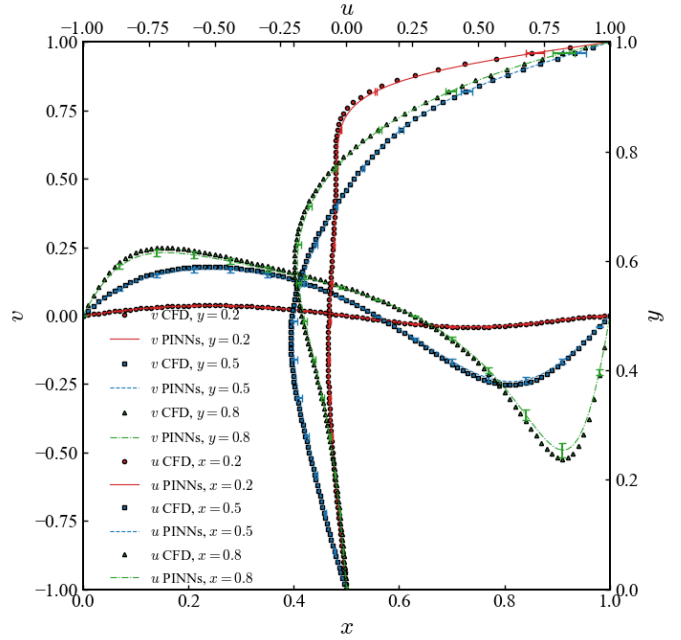


FIG. 9. Comparison of u -velocity profiles along vertical lines ($x = 0.2, 0.5, 0.8$) and v -velocity profiles along horizontal lines ($y = 0.2, 0.5, 0.8$) between PINNs predictions and OpenFOAM 12 results at $Re = 100$. Error bars represent $\pm 5\%$ of the CFD ground truth.

tion region, while Reynolds numbers outside this interval are treated as the *extrapolation region*. This distinction allows for a systematic evaluation of the model's ability to generalize within and beyond the training domain.

Table V summarizes the MSE and R^2 values for the velocity components (u, v) and pressure p across the tested Reynolds numbers, covering both interpolation and extrapolation regimes. Within the interpolation region ($50 \leq Re \leq 300$), the PINNs exhibit excellent performance, characterized by low MSE values on the order of 10^{-4} to 10^{-3} for the velocity components and consistently high R^2 values exceeding 0.95 in most cases. These results demonstrate strong agreement between the PINNs predictions and the CFD reference solutions.

The pressure field exhibits comparatively higher MSE values, which is expected since pressure in incompressible flows is defined up to an arbitrary constant and typically exhibits weaker spatial variation than velocity. After applying mean correction, the PINNs are still able to capture the pressure dis-

tribution accurately, as reflected by R^2 values generally above 0.9 within the interpolation range.

Figure 18 provides a visual summary of the error trends. In the figure, the gray shaded region denotes the interpolation region corresponding to the training range ($50 \leq Re \leq 300$), while the red shaded region represents the extrapolation regime. The left panel shows the variation of MSE with Reynolds number, indicating minimal errors within the interpolation region and a gradual increase as the Reynolds number moves into the extrapolation regime. The right panel presents the corresponding R^2 values, which remain high within the training range and decrease progressively outside it.

As the Reynolds number departs from the interpolation region (e.g., $Re = 10, 30$ and $Re \geq 400$), a noticeable degradation in accuracy is observed. This behavior highlights the inherent challenge of extrapolation in data-driven and physics-informed models, particularly for flows with increased non-linearity and sharper gradients at higher Reynolds numbers.

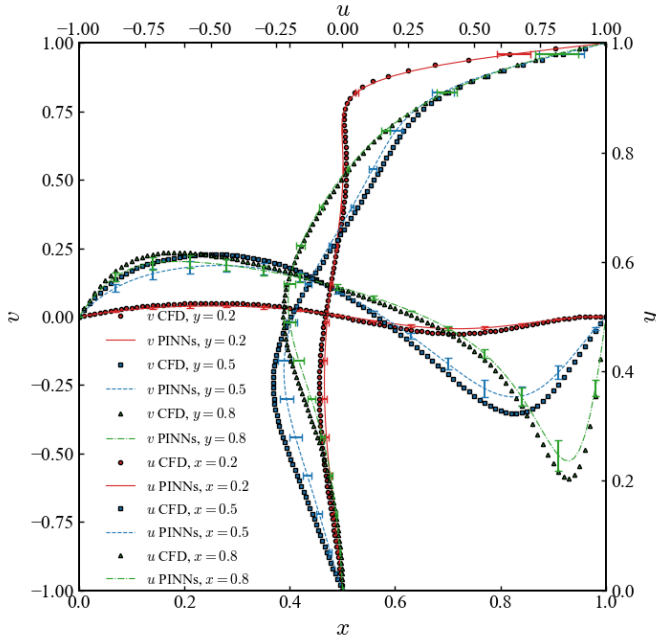


FIG. 10. Comparison of u -velocity profiles along vertical lines ($x = 0.2, 0.5, 0.8$) and v -velocity profiles along horizontal lines ($y = 0.2, 0.5, 0.8$) between PINNs predictions and OpenFOAM 12 results at $Re = 200$. Error bars represent $\pm 10\%$ of the CFD ground truth..

Nevertheless, even in the extrapolation regime, the PINNs maintain reasonable predictive capability, especially for the velocity fields.

These results demonstrate that the proposed PINNs framework achieves high accuracy within the interpolation region and exhibits a graceful degradation in performance outside the training range, confirming its robustness and generalization potential for lid-driven cavity flow simulations.

B. High Reynolds Number Regime (with Transfer Learning)

In this section, the performance of the PINNs framework is examined at higher Reynolds numbers, specifically up to $Re = 2000$, for the lid-driven cavity flow. As observed in the previous section, the predictive capability of standard PINNs degrades as the Reynolds number increases. This degradation is associated with the increasing stiffness of the Navier–Stokes equations at high Reynolds numbers, where convective transport dominates and sharp velocity and vorticity gradients emerge. In this regime, PINNs are known to suffer from spectral bias and optimization difficulties, which limit their ability to represent the wide range of interacting spatial scales³³. In addition, classical results on the predictability of multi-scale fluid systems indicate that errors originating at small or insufficiently constrained scales can rapidly propagate to larger scales, imposing intrinsic limits on achievable predictive accuracy³⁹.

At high Re , the convective terms in the Navier-Stokes equations dominate over the diffusive terms. Consequently,

when minimizing the PDE-based loss function, the optimization landscape becomes heavily influenced by the convection-dominated residuals. This imbalance can cause the optimizer to converge to suboptimal regions of the loss surface where diffusion effects are underrepresented, preventing the network from accurately capturing steep gradients and complex flow structures characteristic of high-Reynolds-number flows.

To address these challenges, supplemental CFD data are incorporated into the PINNs loss function through an additional data loss term, resulting in what we refer to as a *hybrid PINNs* framework. By integrating physics-based constraints with data-driven supervision, this hybrid approach enhances training robustness in convection-dominated regimes. The effectiveness of incorporating sparse or high-fidelity CFD data to improve convergence and stability in such flows has been well documented in the literature^{40–42}, where sparse sensor information is used within physics-informed models to reconstruct key flow features and accelerate learning.

The designed model is trained over a Reynolds number range of $Re \in [500, 1000]$. However, instead of providing CFD data across the entire training range, supervised data are supplied only for a narrow subrange, $Re \in [750, 850]$. This sparse data injection serves to gently guide the neural network toward physically meaningful solutions without overwhelming the physics-based learning process. Even this limited supervision significantly improves the optimization process, leading to faster convergence of the loss function and improved stability during training.

In addition, transfer learning is employed by initializing the network weights using a pretrained model obtained at lower Reynolds numbers. This strategy leverages previously learned physical representations of the flow and has been shown to accelerate convergence and improve solution quality in PINNs^{17,43}. The combined use of transfer learning and sparse CFD data effectively corrects the imbalance between convective and diffusive contributions in the governing equations, steering the optimization toward more accurate minima of the loss landscape.

After training, the model predictions are compared against ground-truth CFD solutions for Reynolds numbers both within the training range, referred to as the *interpolation region*, and outside the training range, referred to as the *extrapolation region*. This evaluation enables a systematic assessment of the model's ability to generalize across Reynolds numbers and demonstrates the effectiveness of the hybrid PINNs framework in capturing high-Reynolds-number flow physics with limited data assistance.

1. Loss Function Design for High Reynolds Numbers

For high Reynolds number cases, the total loss function is augmented with an additional data-driven term to compensate for the dominance of the convective terms in the Navier-Stokes equations. The modified loss function is defined as

$$\mathcal{L} = \lambda_b \mathcal{L}_b + \lambda_{\text{PDE}} \mathcal{L}_{\text{PDE}} + \lambda_D \mathcal{L}_D \quad (16)$$

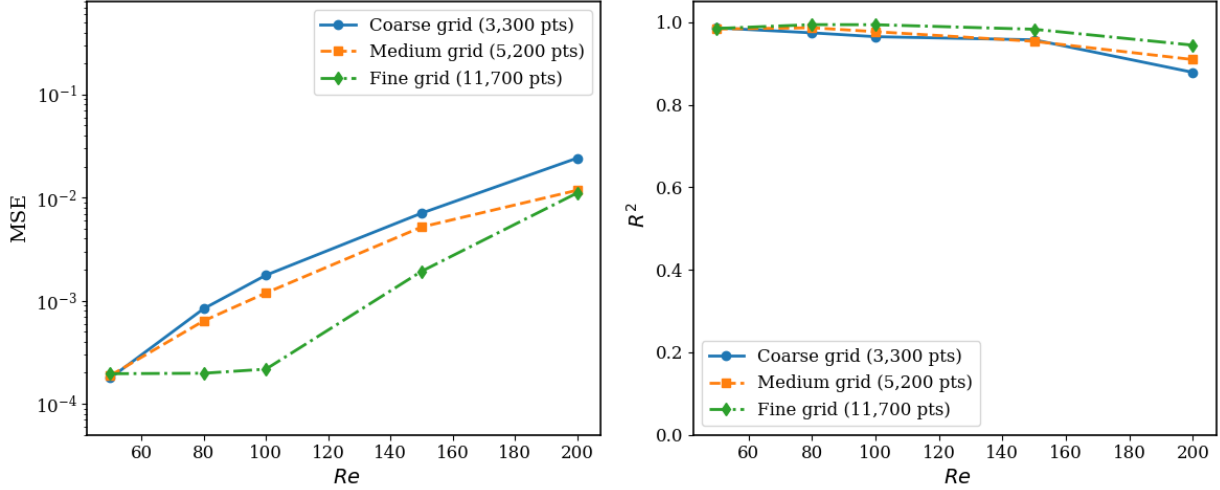


FIG. 11. Influence of collocation-point density on PINNs accuracy for the lid-driven cavity problem. Left: Mean squared error (MSE) of the predicted u velocity fields for coarse (3,300 points), medium (5,200 points), and fine (11,700 points) grids. Right: Coefficient of determination (R^2) for the same grids.

TABLE IV. MSE and R^2 results for different Reynolds numbers. Rows shaded in gray indicate the interpolation region ($50 \leq Re \leq 300$), while unshaded rows correspond to the extrapolation region.

Re	MSE			R^2		
	u	v	p	u	v	p
10	2.74×10^{-3}	2.57×10^{-3}	2.58×10^{-1}	0.9427	0.8687	0.5145
30	4.36×10^{-4}	4.10×10^{-4}	1.03×10^{-2}	0.9908	0.9793	0.8320
50	1.84×10^{-4}	1.84×10^{-4}	2.05×10^{-3}	0.9961	0.9910	0.9170
80	1.11×10^{-4}	1.17×10^{-4}	7.27×10^{-4}	0.9976	0.9946	0.9504
100	1.06×10^{-4}	1.29×10^{-4}	6.39×10^{-4}	0.9977	0.9943	0.9522
150	1.71×10^{-4}	2.99×10^{-4}	7.05×10^{-4}	0.9963	0.9884	0.9526
200	4.12×10^{-4}	6.78×10^{-4}	8.92×10^{-4}	0.9910	0.9762	0.9450
250	8.22×10^{-4}	1.23×10^{-3}	1.10×10^{-3}	0.9821	0.9597	0.9292
300	1.41×10^{-3}	1.94×10^{-3}	1.34×10^{-3}	0.9695	0.9398	0.8918
400	4.14×10^{-3}	4.27×10^{-3}	2.09×10^{-3}	0.9104	0.8766	0.6815
500	1.06×10^{-2}	8.85×10^{-3}	2.73×10^{-3}	0.7702	0.7558	0.4594

where λ_b , λ_{PDE} , and λ_D are weighting coefficients.

The PDE and BC loss retain the same structure as in the pure PINNs formulation and enforces the continuity and momentum equations along with the boundary conditions. To improve accuracy at high Re , a data loss term is introduced using CFD data from OpenFOAM 12:

$$\mathcal{L}_D = \frac{1}{N_D} \sum_{i=1}^{N_d} \left[(u_i^{\text{pred}} - u_i^D)^2 + (v_i^{\text{pred}} - v_i^D)^2 + (p_i^{\text{pred}} - p_i^D)^2 \right] \quad (17)$$

where (u_i^D, v_i^D, p_i^D) denote the reference CFD values and N_D is the number of data points.

This hybrid loss formulation helps stabilize optimization at high Reynolds numbers by guiding the model toward physically meaningful minima while retaining the physics-based structure of the original PINNs framework.

2. Contours of u , v , and p

Contour plots of the horizontal velocity (u), vertical velocity (v), and pressure (p) fields are presented to visually assess the predictive accuracy of the hybrid PINNs framework against high-fidelity CFD reference solutions. The trained PINNs model, informed by sparse CFD data and transfer learning, is used to predict the flow variables, and the resulting fields are directly compared with the corresponding OpenFOAM 12 solutions.

To evaluate both interpolation and extrapolation performance, the contours are plotted at Reynolds numbers $Re = 800$, representing the interpolation region within the training range, and $Re = 300$ and $Re = 1200$, representing the extrapolation region below and above the training interval, respectively. This selection enables a clear visualization of the model's ability to generalize across Reynolds numbers.

Figure 13 presents comparisons of the horizontal velocity (u) contours obtained from the hybrid PINNs model and the

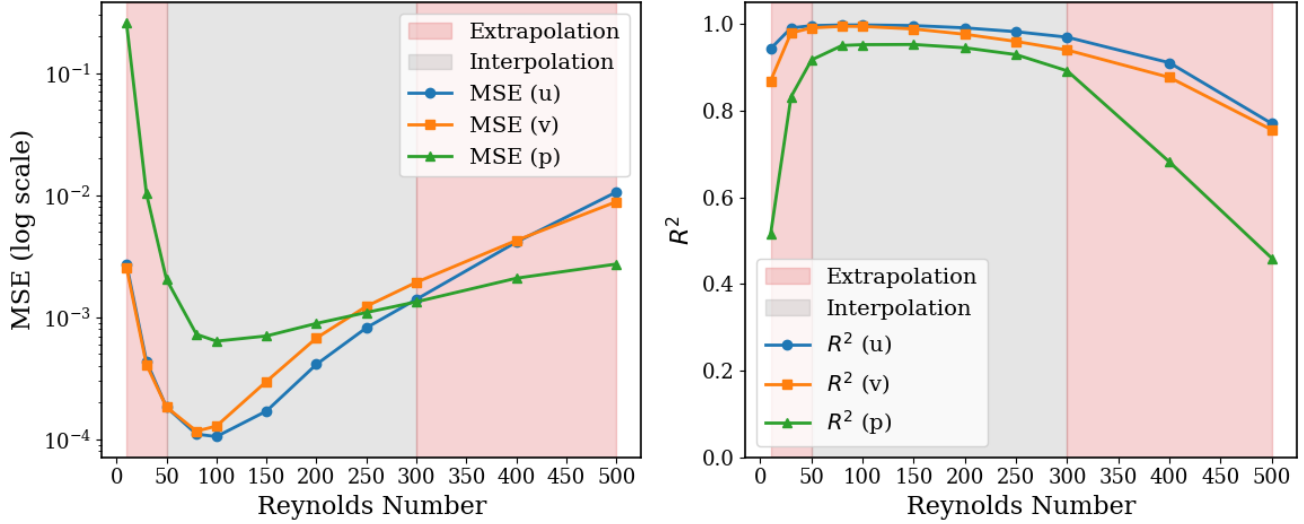


FIG. 12. Quantitative comparison of PINNs predictions with CFD data across different Reynolds numbers. The gray and red regions are for interpolation and extrapolation, respectively. Left: MSE of the predicted velocity components u , v , and pressure p . Right: R^2 comparing PINNs predictions with CFD reference solutions.

OpenFOAM 12 simulations at $Re = 300$, 800 , and 1200 , along with the corresponding absolute error distributions. The error contours illustrate the spatial distribution of prediction errors over the entire computational domain. The u -velocity contours show strong agreement with the CFD reference in both the interpolation and extrapolation regions, with only localized, low-magnitude discrepancies near regions of high shear.

Similarly, Fig. 14 illustrates the contour comparisons for the vertical velocity (v) and pressure (p) fields at the same Reynolds numbers, together with their absolute error fields. The pressure contours exhibit excellent agreement with the CFD solutions in both interpolation and extrapolation regimes, indicating that the hybrid PINNs model successfully captures the global pressure distribution. The vertical velocity (v) field is also predicted accurately within the interpolation region ($Re = 800$). However, in the extrapolation region at higher Reynolds number ($Re = 1200$), the v -velocity contours show moderate deviations from the CFD reference, reflecting the increased sensitivity of the secondary velocity component to extrapolation in convection-dominated flows.

The contour and error visualizations confirm that the hybrid PINNs framework accurately reconstructs the primary flow features across the domain, achieving high fidelity in the interpolation regime and maintaining reasonable predictive accuracy in extrapolation, particularly for the u -velocity and pressure fields.

3. Velocity Profiles

Velocity profiles extracted along selected geometric centerlines of the cavity are used to provide a quantitative assessment of the predictive accuracy of the hybrid PINNs model. These profiles offer a detailed comparison of the local velocity distributions and serve as strong indicators of the effective-

ness of transfer learning in enabling the model to recover the correct flow physics across the computational domain.

Velocity profiles are evaluated at Reynolds numbers corresponding to the center of the training range as well as the extreme points of the training interval, specifically $Re = 500$, 800 , and 1000 . This selection enables a systematic assessment of the model's interpolation capability within the training range and its robustness at the boundaries of the trained Reynolds number space.

Figures 15, 16, and 17 present comparisons of the velocity profiles between the hybrid PINNs predictions and the OpenFOAM 12 reference solutions at Reynolds numbers $Re = 500$, 800 , and 1000 , respectively. Specifically, the horizontal velocity (u) profiles are plotted along vertical lines at $x = 0.3$, 0.5 , and 0.8 , while the vertical velocity (v) profiles are plotted along horizontal lines at $y = 0.3$, 0.5 , and 0.8 .

The error bars shown in the figures correspond to $\pm 7\%$, $\pm 1\%$, and $\pm 3\%$ of the CFD ground truth values for $Re = 500$, 800 , and 1000 , respectively. The PINNs predictions consistently lie within these bounds and exhibit strong agreement with the OpenFOAM 12 results across all sampled locations and Reynolds numbers. This close alignment confirms the robustness of the trained hybrid PINNs model and highlights the benefits of incorporating CFD data through transfer learning for accurately capturing velocity distributions in complex flow regimes.

4. Model Accuracy: Comparison Between CFD and PINNs Predictions

The predictive accuracy of the hybrid PINNs model is quantitatively evaluated by comparing the predicted velocity and pressure fields with high-fidelity CFD solutions obtained using OpenFOAM 12. The assessment is performed over a wide

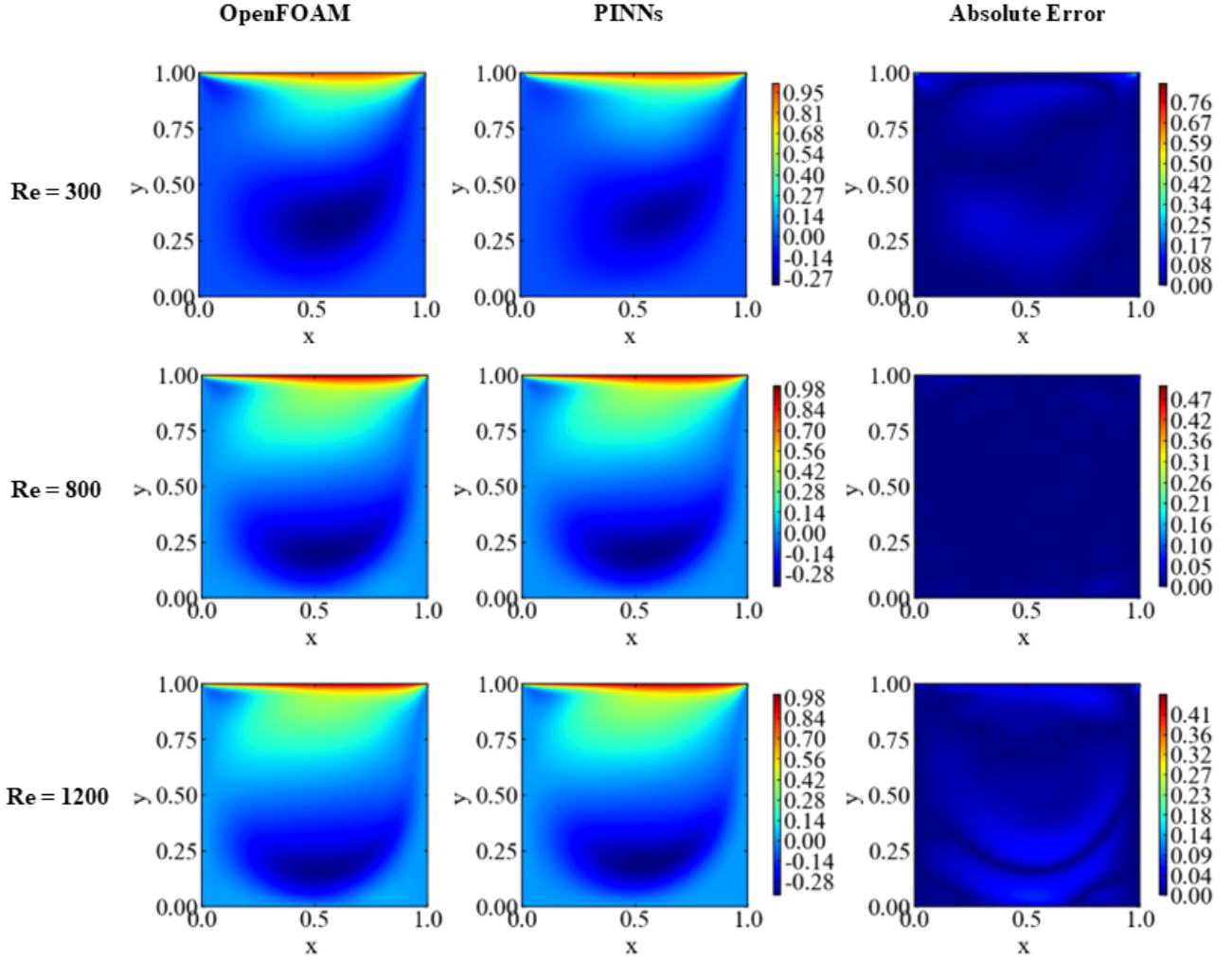


FIG. 13. Comparison of horizontal velocity (u) contours between the hybrid PINNs predictions and OpenFOAM 12 results at $Re = 300, 800$, and 1200 , along with the corresponding absolute error contours.

range of Reynolds numbers to explicitly quantify both the interpolation and extrapolation capabilities of the trained model.

Table V reports the MSE and R^2 values for the horizontal velocity (u), vertical velocity (v), and pressure (p) fields across Reynolds numbers ranging from $Re = 200$ to $Re = 2000$. The Reynolds number interval $Re \in [500, 1000]$, shaded in gray in the table, corresponds to the interpolation region, i.e., the range over which the model was trained. Reynolds numbers outside this interval constitute the extrapolation region.

Within the interpolation region, the hybrid PINNs model demonstrates excellent predictive performance. The MSE values remain consistently low for all three flow variables, reaching minima around the center of the training range. Correspondingly, the R^2 values exceed 0.99 for both velocity components and remain above 0.99 for pressure, indicating that the model accurately reconstructs the CFD solutions throughout the trained Reynolds number space. Notably, the strongest agreement is observed in the subrange $750 < Re < 850$, which

is highlighted as a green-shaded region in Fig. 18. This sub-region corresponds to the Reynolds numbers for which sparse CFD data were explicitly provided during training, underscoring the effectiveness of limited data supervision in guiding the optimization toward physically meaningful solutions.

The extrapolation performance of the model is assessed for Reynolds numbers below $Re = 500$ and above $Re = 1000$, shown as red-shaded regions in Fig. 18. As expected, the prediction error increases gradually as the Reynolds number moves farther away from the training interval. This trend is reflected by increasing MSE values and a corresponding reduction in R^2 scores, particularly at $Re = 1500$ and $Re = 2000$. Nevertheless, even in the extrapolation regime, the model retains reasonable accuracy, with R^2 values remaining above 0.90 for velocity fields and above 0.84 for pressure, demonstrating a robust generalization capability.

Figure 18 visually summarizes these trends by plotting the MSE and R^2 metrics as functions of the Reynolds number,

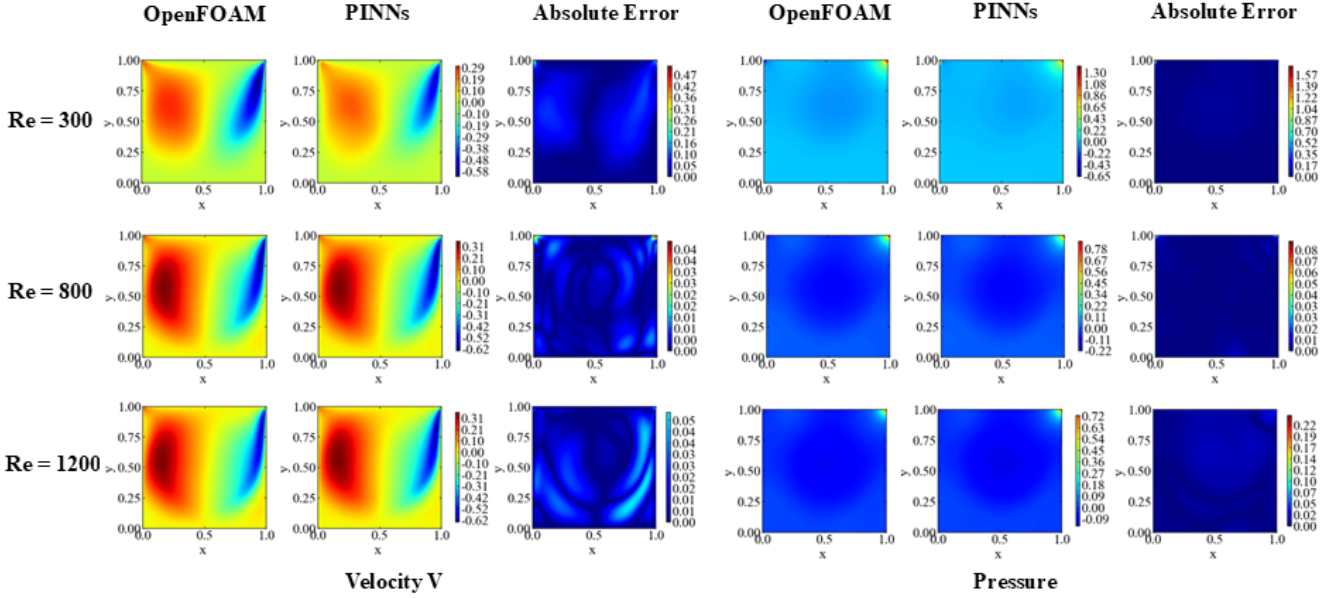


FIG. 14. Comparison of vertical velocity (v) and pressure (p) contours between the hybrid PINNs predictions and OpenFOAM 12 results at $Re = 300, 800$, and 1200 , along with the corresponding absolute error contours.

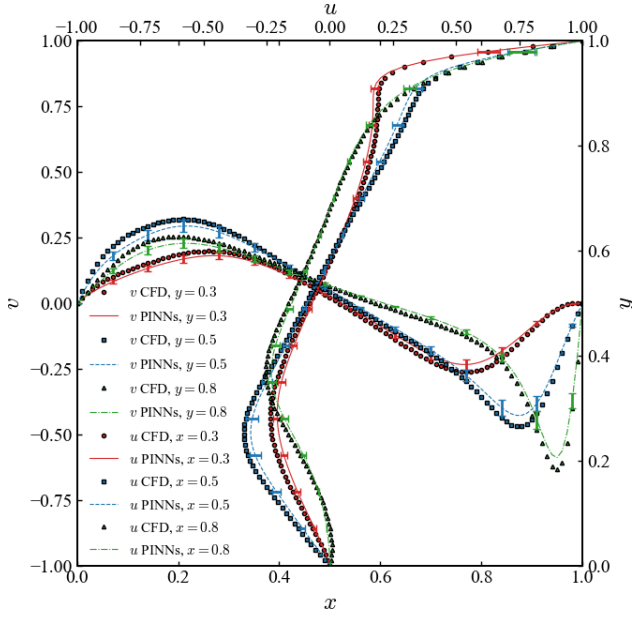


FIG. 15. Comparison of u -velocity profiles along vertical lines ($x = 0.3, 0.5, 0.8$) and v -velocity profiles along horizontal lines ($y = 0.3, 0.5, 0.8$) between PINNs predictions and OpenFOAM 12 results at $Re = 500$. Error bars represent $\pm 7\%$ of the CFD ground truth.

with clear demarcation of the interpolation region, the extrapolation region, and the CFD-assisted subregion. Together, the results confirm that the proposed hybrid PINNs framework not only achieves high accuracy within the training range but also exhibits strong extrapolation performance, highlighting

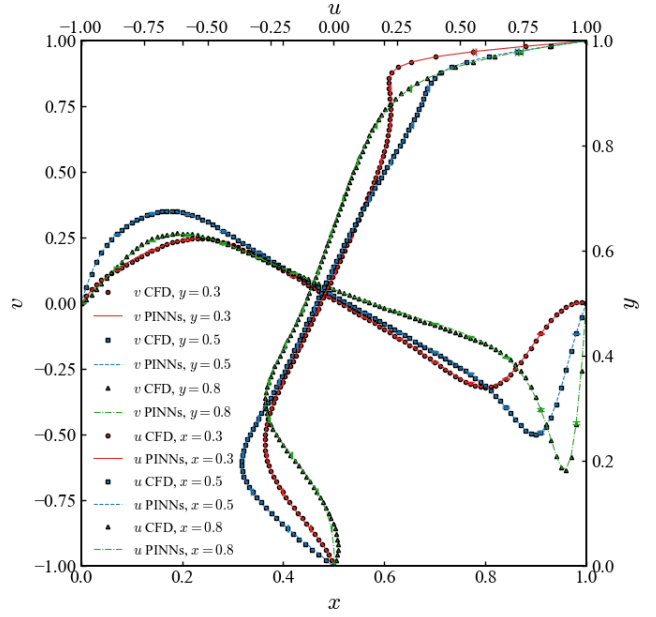


FIG. 16. Comparison of u -velocity profiles along vertical lines ($x = 0.3, 0.5, 0.8$) and v -velocity profiles along horizontal lines ($y = 0.3, 0.5, 0.8$) between PINNs predictions and OpenFOAM 12 results at $Re = 800$. Error bars represent $\pm 1\%$ of the CFD ground truth.

the combined benefits of physics-based learning, sparse CFD data incorporation, and transfer learning in modeling high-Reynolds-number flows.

TABLE V. MSE and R^2 results for different Reynolds numbers. Rows shaded in gray indicate the interpolation region ($500 \leq \text{Re} \leq 1000$), while unshaded rows correspond to the extrapolation region.

Re	MSE			R^2		
	u	v	p	u	v	p
200	2.54×10^{-3}	3.49×10^{-3}	2.31×10^{-3}	0.9490	0.8755	0.5103
300	9.08×10^{-4}	1.78×10^{-3}	1.28×10^{-3}	0.9818	0.9437	0.6355
400	5.23×10^{-4}	8.64×10^{-4}	5.21×10^{-4}	0.9896	0.9746	0.8256
500	2.40×10^{-4}	3.26×10^{-4}	1.36×10^{-4}	0.9952	0.9909	0.9497
600	8.67×10^{-5}	9.60×10^{-5}	2.25×10^{-5}	0.9983	0.9974	0.9910
700	6.96×10^{-5}	2.73×10^{-5}	8.31×10^{-6}	0.9986	0.9993	0.9965
800	6.16×10^{-5}	1.23×10^{-5}	4.57×10^{-6}	0.9988	0.9997	0.9979
900	8.51×10^{-5}	2.55×10^{-5}	6.32×10^{-6}	0.9983	0.9993	0.9970
1000	1.86×10^{-4}	7.82×10^{-5}	1.47×10^{-5}	0.9962	0.9979	0.9925
1200	5.68×10^{-4}	2.90×10^{-4}	3.60×10^{-5}	0.9880	0.9922	0.9796
1500	1.62×10^{-3}	8.61×10^{-4}	8.97×10^{-5}	0.9640	0.9755	0.9396
2000	3.86×10^{-3}	2.15×10^{-3}	1.84×10^{-4}	0.9075	0.9334	0.8425

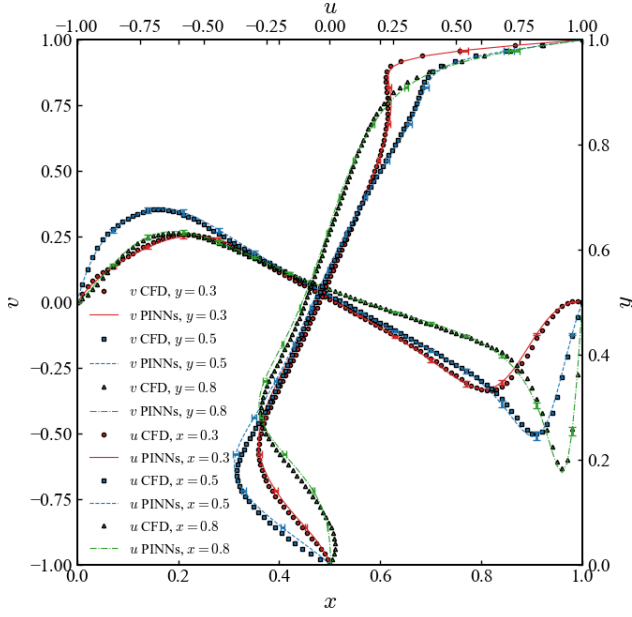


FIG. 17. Comparison of u -velocity profiles along vertical lines ($x = 0.3, 0.5, 0.8$) and v -velocity profiles along horizontal lines ($y = 0.3, 0.5, 0.8$) between PINNs predictions and OpenFOAM 12 results at $Re = 1000$. Error bars represent $\pm 3\%$ of the CFD ground truth.

5. Loss Function Convergence and GPU Utilization

The incorporation of CFD data in the training procedure introduces a data loss component alongside the physics-based loss. It is observed that this hybrid loss formulation leads to faster and more stable convergence compared to pure PINNs. The data-driven guidance effectively constrains the solution space, enabling the network to overcome the optimization challenges associated with highly convective flow regimes. A brief comparison was carried out to evaluate the training performance of PINNs on two hardware setups: an NVIDIA T4 GPU on Google Colab and a 16-core Intel i5 CPU with 64 GB

RAM. The same network architecture was used in all tests, and only the grid size and number of epochs were varied. The results show that GPU training is significantly faster than CPU training. In particular, the T4 GPU provides about a $1.9\times$ speedup compared to the CPU for similar problem settings. This makes GPU acceleration especially useful for larger grid resolutions, where the computational cost of PINNs increases rapidly due to repeated PDE residual calculations.

The training times for both GPU and CPU runs are summarized in Tables VI and VII.

TABLE VI. Training time on Google Colab T4 GPU.

Time (min)	Grid	Epochs	H, N
140	60×60	60,000	10,100
55	80×80	100,000	8,80
70	90×90	100,000	8,80

TABLE VII. Training time on a 16-core Intel i5 CPU (64 GB RAM).

Time (min)	Grid	Epochs	H, N
460	60×60	100,100	10,100
700	60×60	150,000	10,100
750	90×90	50,000	10,100
1260	90×90	100,000	10,100

IV. CONCLUSION

This study systematically examined the use of physics-informed neural networks (PINNs) for the two-dimensional lid-driven cavity flow over a broad range of Reynolds numbers, with particular emphasis on parameterized learning, transfer learning, and the targeted integration of sparse CFD data. A central aspect of the proposed framework is the explicit treatment of the Reynolds number as a continuous input parameter, alongside the spatial coordinates. This formulation enables a single trained network to represent a Reynolds-number-dependent Navier-Stokes solution manifold, allowing

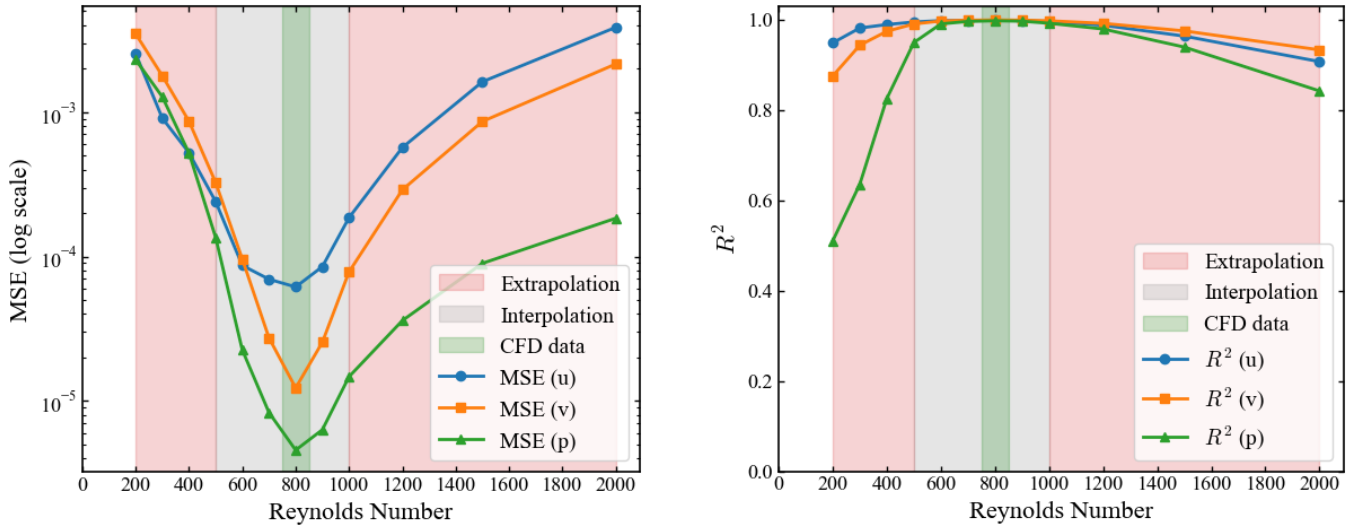


FIG. 18. Quantitative comparison of hybrid PINNs predictions with CFD data across Reynolds numbers. Left: MSE for the predicted horizontal velocity (u), vertical velocity (v), and pressure (p). Right: R^2 relative to CFD reference solutions. The gray-shaded region ($500 \leq Re \leq 1000$) denotes the interpolation (training) range, the green-shaded subregion ($750 < Re < 850$) indicates Reynolds numbers with CFD data assistance, and the red-shaded regions represent extrapolation beyond the training range.

prediction of velocity and pressure fields at previously unseen flow conditions through both interpolation and limited extrapolation in parameter space.

For low Reynolds numbers ($Re \leq 300$), where viscous effects dominate and the governing equations remain relatively well conditioned, pure PINNs trained solely using physics-based loss functions accurately reproduced the velocity and pressure fields without reliance on CFD data. The predicted flow structures, centerline velocity profiles, and pressure distributions showed strong agreement with OpenFOAM 12 reference solutions, demonstrating that parameterized PINNs can serve as accurate and data-efficient solvers in laminar, diffusion-dominated regimes while maintaining physical consistency.

As the Reynolds number increased and the flow became increasingly convection dominated ($Re \geq 500$), the accuracy of pure PINNs deteriorated. This degradation is attributed not to insufficient network capacity but to stiffness in the Navier-Stokes equations and optimization imbalance associated with sharp velocity gradients and multiscale flow features. These effects hinder convergence when the solution is constrained solely through physics-based residuals. To address this limitation, a hybrid PINNs framework was introduced that combines transfer learning with sparse supervision from high-fidelity CFD data.

By supplying CFD data only within a narrow Reynolds-number subrange ($750 < Re < 850$) while training the model over a wider interval ($Re \in [500, 1000]$), the optimization process was effectively guided toward physically meaningful solutions. This targeted data assistance significantly improved stability and convergence while preserving the physics-informed structure of the model. The hybrid framework exhibited excellent interpolation performance across the trained Reynolds-number range, with consistently low pre-

diction errors and strong agreement with CFD reference solutions. The highest accuracy was observed near the data-assisted region, highlighting the role of sparse data in anchoring the learned solution manifold.

Extrapolation beyond the training interval revealed a gradual and physically reasonable degradation in accuracy with increasing distance from the trained Reynolds-number range. The hybrid PINNs model retained robust predictive capability for the horizontal velocity and pressure fields, while larger deviations were observed in the vertical velocity component at higher Reynolds numbers. Nevertheless, contour visualizations and centerline profiles confirmed that key flow features—including recirculation zones, corner vortices, and sharp velocity gradients—were accurately captured across both interpolation and extrapolation regimes, with errors remaining spatially localized and of low magnitude.

While the lid-driven cavity flow provides a canonical benchmark for assessing numerical methods for incompressible Navier-Stokes equations, it is emphasized that the cavity serves here as a testbed rather than the target application. The proposed parameterized PINNs framework is general and may be extended to other classes of flows governed by similar conservation laws. In particular, the explicit inclusion of governing non-dimensional parameters enables straightforward extension to problems involving additional dimensionless groups, such as the Prandtl, Grashof, or Rayleigh numbers, as well as to families of boundary conditions and forcing configurations. This capability is particularly relevant for reduced-order modeling and parametric studies, where efficient exploration of high-dimensional parameter spaces is required and repeated high-fidelity CFD simulations become computationally prohibitive.

Taken together, the results demonstrate that pure PINNs are well suited for low-Reynolds-number laminar flows, whereas

hybrid PINNs augmented with transfer learning and sparse CFD data provide a robust and scalable approach for moderate Reynolds-number regimes. Treating the Reynolds number as a continuous input parameter enables efficient parametric flow prediction using a single unified model, reducing the need for repeated retraining across operating conditions. Although the present study focused on a steady, two-dimensional benchmark flow, the proposed framework provides a foundation for developing reduced-order, physics-consistent Navier-Stokes solvers that bridge conventional CFD and data-assisted modeling.

V. REFERENCES

- ¹P. N. Shankar and M. D. Deshpande, “Fluid mechanics in the driven cavity,” *Annual Review of Fluid Mechanics* **32**, 93–136 (2000).
- ²U. Ghia, K. N. Ghia, and C. T. Shin, “High-re solutions for incompressible flow using the navier–stokes equations and a multigrid method,” *Journal of Computational Physics* **48**, 387–411 (1982).
- ³O. Botella and R. Peyret, “Benchmark spectral results on the lid-driven cavity flow,” *Computers & Fluids* **27**, 421–433 (1998).
- ⁴E. Erturk, T. C. Corke, and C. Gökcöl, “Numerical solutions of 2-d steady incompressible driven cavity flow at high reynolds numbers,” *International Journal for Numerical Methods in Fluids* **48**, 747–774 (2005).
- ⁵E. Erturk and C. Gökcöl, “Fourth-order compact formulation of navier–stokes equations and driven cavity flow at high reynolds numbers,” *International Journal for Numerical Methods in Fluids* **50**, 421–436 (2006).
- ⁶M. Raissi, P. Perdikaris, and G. E. Karniadakis, “Physics-informed neural networks: A deep learning framework for solving forward and inverse problems involving nonlinear partial differential equations,” *Journal of Computational Physics* **378**, 686–707 (2019).
- ⁷M. Raissi, A. Yazdani, and G. E. Karniadakis, “Hidden fluid mechanics: A navier–stokes informed deep learning framework for assimilating flow visualization data,” arXiv preprint (2018), 10.48550/arXiv.1808.04327, arXiv:1808.04327 [cs.CE].
- ⁸S. Yang, Z. Jiang, J. Wang, and L. Zhang, “A data-driven reduced-order model framework for predicting turbulent channel flows,” *Physics of Fluids* **37**, 025146 (2025).
- ⁹A. Roy, A. Mukherjee, B. Prasad, and A. K. Nayak, “A computational analysis of flow dynamics and heat transfer in a wavy patterned channel using physics-informed neural networks,” *Physics of Fluids* **37**, 025416 (2025).
- ¹⁰C. Prieto, J. Huang, S. Ansari, and K. Schell, “Physics-informed neural network for open channel flow velocity prediction,” *Physics of Fluids* **37**, 025314 (2025).
- ¹¹K. Duraisamy, G. Iaccarino, and H. Xiao, “Turbulence modeling in the age of data,” arXiv preprint (2018), 10.48550/arXiv.1804.00183, arXiv:1804.00183 [physics.flu-dyn].
- ¹²S. L. Brunton, B. R. Noack, and P. Koumoutsakos, “Machine learning for fluid mechanics,” *Annual Review of Fluid Mechanics* **52**, 477–508 (2020).
- ¹³K. Cai and J. Wang, “Physics-informed neural networks for solving incompressible navier–stokes equations in wind engineering,” *Physics of Fluids* **36**, 121303 (2024).
- ¹⁴E. Kharazmi, Z. Zhang, and G. E. Karniadakis, “hp-vpinns: Variational physics-informed neural networks with domain decomposition,” *Computer Methods in Applied Mechanics and Engineering* **374**, 113547 (2021).
- ¹⁵S. Li and X. Feng, “Dynamic weight strategy of physics-informed neural networks for the 2d navier–stokes equations,” *Entropy* **24**, 1254 (2022).
- ¹⁶P. Chen and X. Zhao, “Enhancing the performance of hard-constrained gradient-enhanced physics-informed neural networks using a residual adaptive sampling method,” *Physics of Fluids* **37**, 107129 (2025).
- ¹⁷Y. Wang, J. Bai, M. S. Eshaghi, C. Anitescu, X. Zhuang, T. Rabczuk, and Y. Liu, “Transfer learning in physics-informed neural networks: Full fine-tuning, lightweight fine-tuning, and low-rank adaptation,” arXiv preprint (2025), arXiv:2502.00782 [cs.LG].
- ¹⁸N. Geneva and N. Zabaras, “Modeling the dynamics of pde systems with physics-constrained deep auto-regressive networks,” *Journal of Computational Physics* **403**, 109056 (2020).
- ¹⁹L. Sun, H. Gao, S. Pan, and J. Wang, “Surrogate modeling for fluid flows based on physics-constrained deep learning without simulation data,” *Computer Methods in Applied Mechanics and Engineering* **361**, 112732 (2020).
- ²⁰X. Meng, Z. Li, D. Zhang, and G. E. Karniadakis, “Ppinn: Parareal physics-informed neural network for time-dependent pdes,” *Computer Methods in Applied Mechanics and Engineering* **370**, 113250 (2020).
- ²¹A. D. Jagtap, K. Kawaguchi, and G. E. Karniadakis, “Adaptive activation functions accelerate convergence in deep and physics-informed neural networks,” *Journal of Computational Physics* **404**, 109136 (2020).
- ²²F. M. White, *Viscous Fluid Flow* (McGraw-Hill, 2006).
- ²³H. Schlichting and K. Gersten, *Boundary-Layer Theory* (Springer, 2017).
- ²⁴H. G. Weller, G. Tabor, H. Jasak, and C. Fureby, “A tensorial approach to computational continuum mechanics using object-oriented techniques,” (1998).
- ²⁵H. Jasak, “Openfoam: A c++ library for complex physics simulations,” in *International Workshop on Coupled Methods in Numerical Dynamics (CW2007)* (Birmingham, UK, 2007) invited lecture.
- ²⁶A. B. Cortes and J. D. Miller, “Numerical experiments with the lid driven cavity flow problem,” *Computers & Fluids* **23**, 1005–1027 (1994).
- ²⁷R. Clements, J. Ellis, G. Hassall, S. Horsley, and G. Tabor, “Plane-wave decomposition and randomised training: a novel path to generalised physics-informed neural networks for simple harmonic motion,” *Machine Learning: Science and Technology* **4**, 045038 (2025).
- ²⁸Y. LeCun, L. Bottou, G. B. Orr, and K.-R. Müller, “Efficient backprop,” *Neural Networks: Tricks of the Trade* , 9–48 (2012).
- ²⁹X. Glorot and Y. Bengio, “Understanding the difficulty of training deep feedforward neural networks,” in *Proceedings of the 13th International Conference on Artificial Intelligence and Statistics (AISTATS 2010)*, Vol. 9 (PMLR, 2010) pp. 249–256.
- ³⁰G. E. Karniadakis, P. Perdikaris, M. Raissi, and L. Yang, “Physics-informed machine learning,” *Nature Reviews Physics* **3**, 422–440 (2021).
- ³¹D. P. Kingma and J. Ba, “Adam: A method for stochastic optimization,” *International Conference on Learning Representations (ICLR)* (2015).
- ³²J. Nocedal and S. J. Wright, *Numerical Optimization* (Springer, 2006).
- ³³S. Wang, X. Yu, and P. Perdikaris, “Understanding and mitigating gradient flow pathologies in physics-informed neural networks,” *SIAM Journal on Scientific Computing* **43**, A3055–A3081 (2021).
- ³⁴Y. Shin, J. Darbon, and G. E. Karniadakis, “On the convergence of physics informed neural networks for linear second-order elliptic and parabolic type pdes,” *Communications in Computational Physics* **28**, 2042–2074 (2020).
- ³⁵S. Mishra and R. Molinaro, “Estimates on the generalization error of physics-informed neural networks for approximating pdes,” *IMA Journal of Numerical Analysis* **43**, 1–43 (2022).
- ³⁶S. Wang, Y. Teng, and P. Perdikaris, “When and why pinns fail to train: A neural tangent kernel perspective,” *Journal of Computational Physics* **449**, 110768 (2022).
- ³⁷F. Hafezianzadeh, M. Biagooi, and S. Nedaaee Oskooe, “Physics informed neural network for charged particles surrounded by conductive boundaries,” *Scientific Reports* **13**, 14072 (2023).
- ³⁸M. L. Mamud, M. K. Mudunuru, S. Karra, and B. Ahmed, “Quantifying local and global mass balance errors in physics-informed neural networks,” *Scientific Reports* **14**, 15541 (2024).
- ³⁹E. N. Lorenz, “The predictability of a flow which possesses many scales of motion,” *Tellus* **21**, 289–307 (1969).
- ⁴⁰M. Raissi, “Deep hidden physics models: Deep learning of nonlinear partial differential equations,” *Journal of Machine Learning Research* **19**, 1–24 (2019).
- ⁴¹L. Yang, X. Meng, and G. E. Karniadakis, “B-pinns: Bayesian physics-informed neural networks for forward and inverse problems with noisy data,” *Journal of Computational Physics* **425**, 109913 (2021).
- ⁴²M. Y. Hosseini and Y. Shiri, “Flow field reconstruction from sparse sensor measurements with physics-informed neural networks,” *Physics of Fluids* **36**, 073606 (2024).
- ⁴³K. Prantikos, S. Chatzidakis, L. H. Tsoukalas, and A. Heifetz, “Physics-informed neural network with transfer learning (tl-pinn) based on domain similarity measure for prediction of nuclear reactor transients,” *Scientific Reports* **13**, 16840 (2023).